RESEARCH ARTICLE

ELECTRON MICROSCOPY

Visualizing nanoparticle surface dynamics and instabilities enabled by deep denoising

Peter A. Crozier[1]*, Matan Leibovich[2], Piyush Haluai[1], Mai Tan[1], Andrew M. Thomas[3], Joshua Vincent[1], Sreyas Mohan[4], Adria Marcos Morales[4], Shreyas A. Kulkarni[4], David S. Matteson[5], Yifan Wang[1], Carlos Fernandez-Granda[2,4]*

Materials functionalities may be associated with atomic-level structural dynamics occurring on the millisecond timescale. However, the capability of electron microscopy to image structures with high spatial resolution and millisecond temporal resolution is often limited by poor signal-to-noise ratios. With an unsupervised deep denoising framework, we observed metal nanoparticle surfaces (platinum nanoparticles on cerium oxide) in a gas environment with time resolutions down to 10 milliseconds at a moderate electron dose. On this timescale, many nanoparticle surfaces continuously transition between ordered and disordered configurations. Stress fields can penetrate below the surface, leading to defect formation and destabilization, thus making the nanoparticle fluxional. Combining this unsupervised denoiser with in situ electron microscopy greatly improves spatiotemporal characterization, opening a new window for the exploration of atomic-level structural dynamics in materials.

Nanoparticle surface structural dynamics, sometimes referred to as fluxionality, may play an important role in regulating functionalities such as diffusion, reactivity, and catalysis, but the atomic-level processes are not well understood (*1*). The importance of atomic-level structural dynamics is well established for protein functionality but has been less discussed in materials (*2*). Recent works have shown that surface fluxionality may be directly correlated with catalytic functionality (*3*, *4*). For example, fluxional effects at the atomic level were found to be correlated with CO oxidation activity in a Pt on a CeO_2 catalyst, but the spatiotemporal details were obscured by poor signal-to-noise ratios (SNRs) (*3*). Atom dynamics consist of different types of motions ranging from very fast vibrations to slower migrations. If we could locally characterize atom migration (which depends on temperature) on millisecond timescales, this would deepen our understanding of functionalities. For example, in heterogeneous catalysis, reaction rates per active site are typically in the range of 1 to 100/s and may be associated with the formation of short-lived metastable surface structures that exist on the tens of milliseconds timescale. However, atomic resolution characterization of nanoparticle surface dynamics is challenging because it requires both high spatial and temporal resolution. Ultrafast transmission electron microscopy (TEM) can achieve picosecond temporal resolution but is limited to nanometer spatial resolution (*5*–*7*). Fortunately, the high readout rates of new electron detectors could allow conventional TEM to visualize atomic structures on a millisecond timescale. Unfortunately, the need to reduce electron beam damage to the sample makes it necessary to limit the electron dose rates, yielding millisecond images that are dominated by noise, which obscures the structural details. Here, we show that a newly developed unsupervised denoising framework based on deep learning enables observations of metal nanoparticle surfaces in a gas environment with time resolutions down to 10 ms at a moderate electron dose. On this timescale, we find that many nanoparticle surfaces continuously transition between ordered and disordered configurations. The associated stress fields can penetrate below the surface, which leads to defect formation and destabilization and makes the entire nanoparticle fluxional.

The concept of fluxionality, in which a system rapidly moves through different isomers, was first discussed for organometallic molecules in the 1950s, as summarized by Cotton (*8*). In the early days of nanoscience, there was interest in fluxional behavior of nanoparticles due in part to observations performed on the newly developed atomic-resolution electron microscopes (*9*). However, older, less-sensitive electron detector technology limited temporal resolutions to ~100 ms and required large electron dose rates ($>10^4$ e Å^2 s^{-1}). The desire to understand structure and functionality in catalytic nanoparticles has driven the continued development of gas and liquid cell TEM (*10*–*13*). However, to limit beam damage, the timescale for much of the reported atomic structural dynamics is often minutes (*14*, *15*). Recently, time resolutions on the order of 10 ms have been reported, but they used high electron dose rates ($\geq 10^4$ e$^-$ Å^{-2} s^{-1}) (*16*, *17*). Here, we used the power of machine learning to reduce the electron dose rate by at least an order of magnitude (~10^3 e$^-$ Å^{-2} s^{-1}) while achieving temporal resolutions of ~10 ms and spatial resolutions of 1 Å. This enabled us to explore the challenging issue of surface dynamics in metal particles.

To address the image noise challenge, we propose a denoising framework based on artificial intelligence (AI), which enables the recovery of atomic-resolution information from noisy images. AI models based on neural networks have achieved impressive results for natural images but often require training datasets with ground-truth clean images (*18*, *19*). Simulating such datasets is challenging; in fact, it is often impossible when the goal of denoising is scientific discovery. We propose a fully unsupervised framework to train and evaluate AI-powered denoising models using exclusively real noisy data (*20*). The framework enabled recovery of atomic-resolution information from TEM data, improving the SNR by a factor of almost 40 at a spatial resolution of 1 Å and time resolution near 10 ms. This enhanced time resolution revealed that supposedly stable, low-energy nanoparticle surfaces can display highly active atom dynamics, triggering instabilities that result in rapid structural fluctuations. The spatiotemporal capability enabled by the proposed AI framework substantially enhances our ability to explore surface dynamics and the evolution of metastable states in nanoparticles at the atomic level, offering insights into their evolving structures.

Data collection and noise processing

For this investigation, we explored the structural dynamics of Pt particles supported on CeO_2 in a CO environment at room temperature. CO interacts strongly with Pt surfaces, with a binding energy of ~1.5 eV and a migration energy of ~0.02 eV (*21*, *22*). The CO surface coverage exceeds 50% even at the modest pressures of 10^{-4} to 10^{-2} Torr used in the current experiment (*23*). To investigate the dynamics, we recorded movies from a Pt/CeO_2 sample with an electron dose rate of 2000 e$^-$ Å^{-2} s^{-1} and a readout rate of 75 frames/s (see movies S1 and S4 in the supplementary materials, section 8), corresponding to a single frame exposure time of 13 ms (individual frames had an electron dose of 26 e$^-$ Å^{-2} s^{-1} and the dose per pixel was 0.2 e$^-$). Each movie was composed of ~1000 to 2000 frames (3500 × 3500 pixels in size) with an SNR (measured in the vacuum) of ~0.45,

---

[1]Materials Science and Engineering, School for Engineering of Matter, Transport & Energy, Arizona State University, Tempe, AZ, USA. [2]Courant Institute of Mathematical Sciences, New York University, New York, NY, USA. [3]Department of Statistics & Actuarial Science, University of Iowa, Iowa City, IA, USA. [4]Center for Data Science, New York University, New York, NY, USA. [5]Department of Statistics & Data Science, Cornell University, Ithaca, NY, USA.
***Corresponding author. Email: crozier@asu.edu (P.A.C.); cfgranda@cims.nyu.edu (C.F.-G.)**

which obscured much of the surface structure in the raw data and made it impossible to observe the underlying dynamics (see the supplementary materials, section 2, for more details).

To process the low-SNR data, we leverage a deep-learning model trained and evaluated exclusively on the same real noisy data. The model is based on recently developed unsupervised deep video denoiser (UDVD), (*20*, *24*) trained to estimate each noisy pixel value using the surrounding spatiotemporal neighborhood but without considering the noisy pixel itself (Fig. 1A). This blind-spot structure, which was enforced through a specialized architectural design, was critical because it prevented the model from learning to trivially map the input to the output directly. Instead, the denoiser learned to estimate the underlying clean image structure without overfitting the noise. Effective denoising occurs provided (i) each pixel in the clean image is correlated with if the surrounding pixels, which is the case if the spatial sampling is sufficiently high with respect to the features of interest (e.g., lattice fringes), and (ii) the noise is spatially and temporally uncorrelated (see the supplementary materials, section 41; see part 4 for an analysis of the spatiotemporal correlation in the noise). UDVD combined several convolutional neural networks with a UNet architecture to process multiple frames at the same time, which enabled it to exploit temporal patterns and multiscale structure (see the supplementary materials, section 1 for additional details). The results achieved by the denoiser are shown in Fig. 1, B and C. After denoising, the atomic structure of the nanoparticles, including the surface, was clearly resolved, showcasing the advantage of unsupervised denoising for scientific discovery.

To evaluate the performance of UDVD, we applied a recently developed unsupervised evaluation metric: the unsupervised peak SNR (uPSNR) (*20*). This metric is computed by using held-out adjacent noisy frames combined with a correction term (Fig. 1, D and E) that yields an unbiased, consistent estimate of the true PSNR, under the assumption that the noise is independent across frames (this is approximately true, as shown in the supplementary materials, section 1). An additional qualitative evaluation of the denoised output

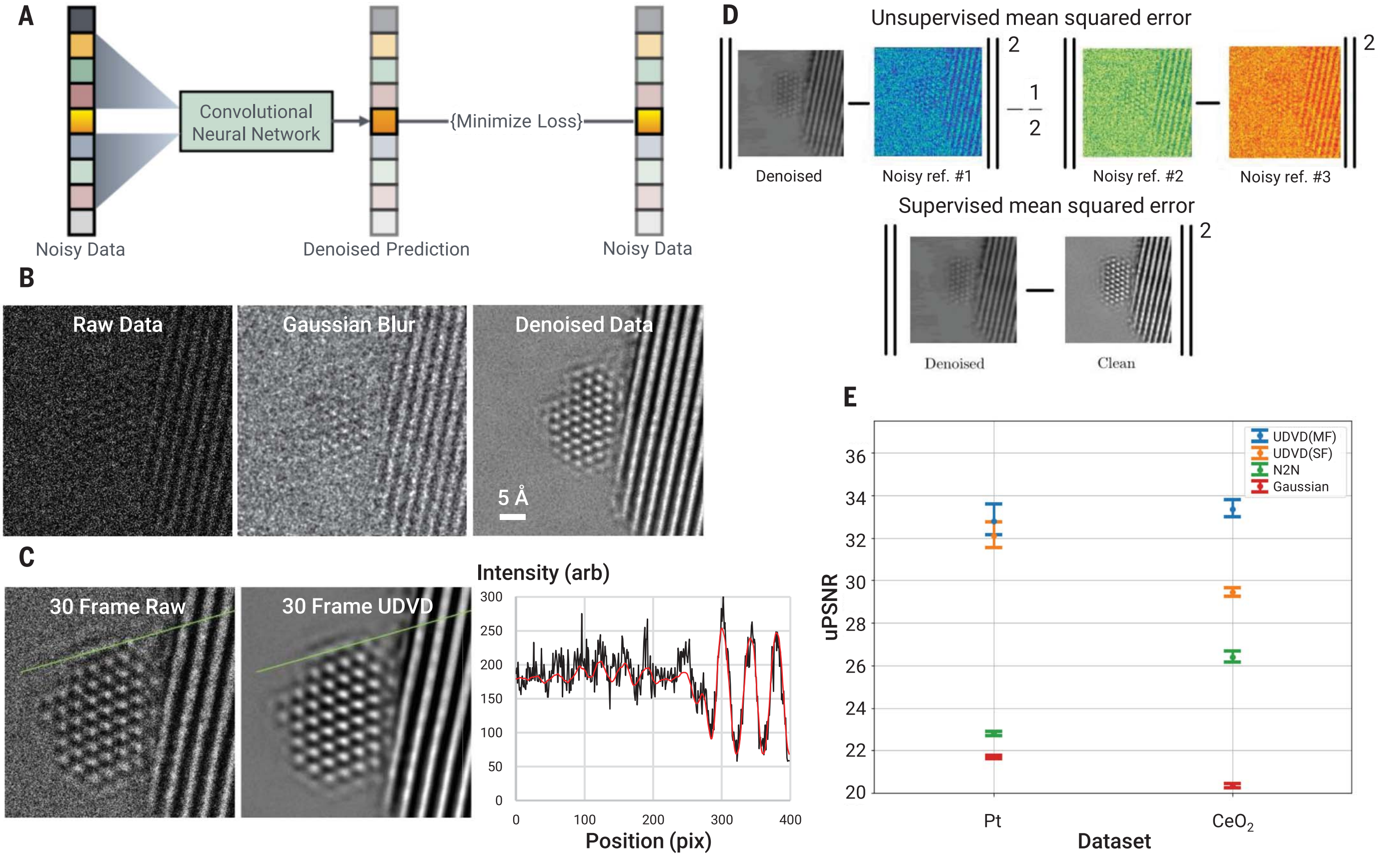

Fig. 1. Unsupervised deep denoising methodology. (**A**) The proposed UDVD learns to remove noise from noisy datasets without access to ground-truth clean images. A deep convolutional neural network is trained to estimate each noisy pixel from its spatiotemporal surrounding but without using the noisy pixel itself. Because the noisy component of the pixel is unpredictable, the network learns to estimate the underlying clean signal. (**B**) Example of denoising results showing the structure of the Pt nanoparticle in a CO atmosphere at room temperature. Left, raw data (13-ms exposure time). Right, same frame after UDVD denoising. Middle, raw frame after Gaussian blur filter for noise reduction. (**C**) Comparison of summed data and denoised data of the 30-frame sum. The surface structures look very similar. Intensity linescans along green lines in images is graphed on the right showing similar intensity variations for the denoised (red trace) and raw (black trace line) data. (see the supplementary materials, section 2). (**D**) To perform quantitative evaluation of unsupervised denoisers, we propose a metric called unsupervised mean squared error (uMSE), which is computed exclusively from noisy data. The uMSE was obtained by comparing the denoised image with an adjacent noisy frame and adding a correction term computed from two additional noisy frames (top row). If the signal content across the noisy frames is consistent and the noise is independent, the uMSE is an unbiased consistent estimator of the supervised MSE between the denoised image and the underlying clean signal (bottom row). (**E**) Comparison of the performance of a single-frame and multiframe version of UDVD against a traditional baseline based on Gaussian filtering (Gaussian) and an alternative unsupervised method known as Neighbor2Neighbor (*1*). The metric was the uPSNR, which equals the logarithm of the uMSE. UDVD achieved a statistically significant superior performance for two datasets containing CeO_2 and Pt nanoparticles. Section 1 of the supplementary materials provides additional details about the models and datasets.

was performed by comparing a temporal average of the raw and denoised data. Figure 1C shows that there is reasonable agreement between the two temporal averages. Further details on training and evaluation of the denoiser output from generating nanoparticle surface structure are provided in the supplementary materials, sections 1 and 2. Based on the vacuum region, the SNR in the UDVD output was ~16.5, which was improved by a factor of ~36 compared with the raw data. To achieve a similar improvement through counting statistics alone would require an increase in beam current or acquisition time by a factor of 1300. Increasing the beam current by such a large factor would destroy the material, whereas increasing the acquisition time by this factor would destroy the time resolution. This result demonstrates the power of the proposed denoising framework (for a more detailed discussion on the role of exposure time for detecting short-lived surface structures, see the supplementary materials, section 7).

Denoised imaging results

The denoiser revealed new dynamics on nanoparticle surfaces. A typical evolution of a 1.2-nm Pt nanoparticle surface supported on a (100) face of a CeO_2 during exposure to 10^{-4} Torr of CO at room temperature is shown in Fig. 2, A to F. The first image at t = 0 s shows the particle in a (110) zone axis with crystallographic terminations corresponding to (111) surfaces. The particle underwent rotation, and its evolved shape led to the formation of a (100) facet. The presence of (111) and (100) crystallographic facets corresponds to the low-energy Winterbottom shape for Pt nanoparticles (*25*). The electron beam will always influence observations in the electron microscope. In this case, section 3 of the supplementary materials addresses this issue and compares energy transfers from the electron beam and thermal processes for Pt surface migration. The calculations show that thermally activated Pt jumps are 10^6 times more likely than electron beam activated jumps, suggesting that the structural fluctuations are predominantly the result of thermal processes.

The high spatiotemporal resolution images revealed diffuse contrast that appeared to “float” above the crystallographic terminations. This component constantly changed in time and space, and a layered chimney structure (labeled in Fig. 2D) is a pronounced example in which despite the nanoparticle being in a zone axis orientation with clearly resolved atomic columns, the chimney structure did not show atomic column contrast (see movies S2 and S3 in the supplementary materials, section 8). This external surface layer was not an artifact of denoising and could also be seen (after suitable averaging) in the raw data (see the supplementary materials, section 4).

Even low-energy (111) facets often had diffuse layers present a substantial fraction of the time. An example from a different particle in which the diffuse surface layer transformed to an ordered bulk terminated-like (111) Pt surface is shown in Fig. 2, G and H. This transformation implied that the diffuse layer, which we call an adlayer, was primarily associated with Pt atoms, but the atoms were neither stationary nor in bulk terminated lattice sites. The electron scattering from CO is much smaller than that from Pt, so the contribution to the diffuse layer signal from CO is not apparent. Consideration of the image contrast suggests (see the supplementary materials, section 7) that similar numbers of atoms are present in rows C and D in Fig. 2, G and H). As shown by Fig. 2 and the associated images in the supplementary materials, section 4, and movies S2, S3, S5, S6, and S7 in the supplementary materials, section 8, the surface is constantly transforming between ordered crystallographic terminations and disordered adlayers on the nanoparticles studied here. Occasionally, the adlayer is associated with the nucleation or dissolution of a crystalline layer on the nanoparticle, whereas other times, an existing crystalline layer transforms to an adlayer and then back to a crystalline layer, as seen in Figs. 2 and 3.

Adlayers composed of diffusing atoms have been reported during thin film growth and the particle sintering that occurs through Ostwald ripening, but we are not aware that this phenomenon has been directly observed on nanoparticles. In Ostwald ripening of supported metal particles, adatoms diffuse on the metal surface, detach from the particles, and migrate across the support to join other larger particles (*26*). In the present case, the strong interaction with CO disrupted metal-metal surface bonds, which increased the likelihood that Pt atoms detached from lattice sites and migrated. Moreover, most nanoparticles would not have the correct number of atoms to form complete (111) and (100) layers to make the perfect Winterbottom shapes. This incomplete layer filling would increase the concentration of low-coordination Pt atoms at step edges and corners sites, which would make adatom detachment more facile. Once the atoms detached from crystal lattice sites, they would likely be highly mobile. For example, the migration energy of Pt on Pt(111) surface is ~0.3 eV, which could result in millions of jumps per second at room temperature (*27*) (see the supplementary materials, section 3).

Strain effects and fluxionality

The surface instabilities generate dynamic strain fields that penetrate below the surface and may trigger disruptions of subsurface

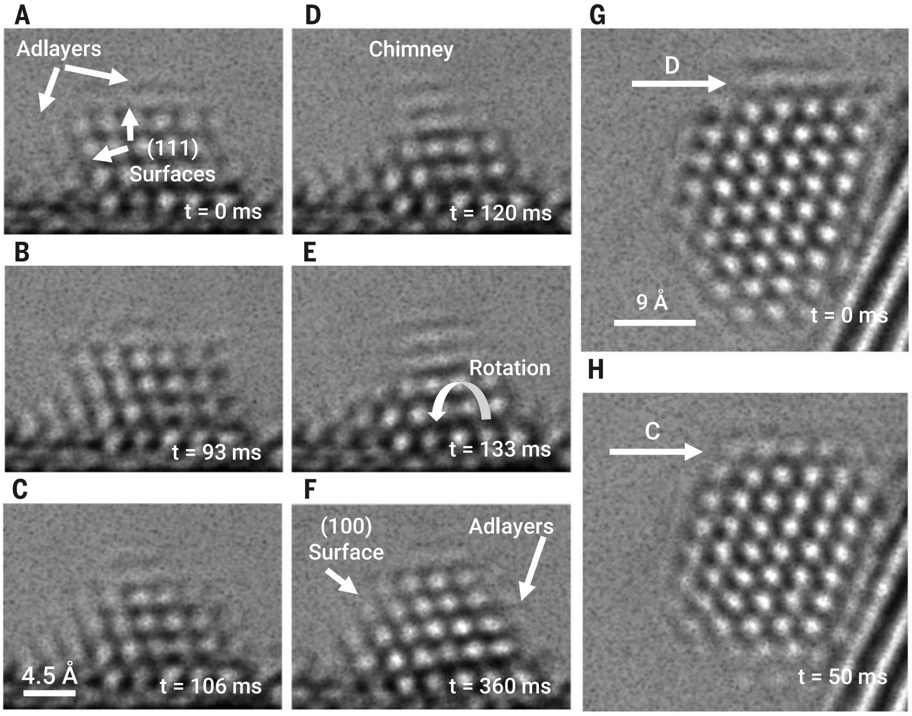

Fig. 2. Surface dynamics in Pt particles. (**A** to **F**) Variation in the surface of a 1.2-nm Pt particle in a CO atmosphere during a time period of 360 ms. The diffuse contrast at the surface of the nanoparticle are the dynamic adlayers of moving atoms. Rapid surface diffusion caused particle shape evolution, such as the formation of metastable chimney structures and (100) facets. (**G** and **H**) Two-nanometer particle showing a disordered fluxional adlayer (D) transforming into a (111) crystallographic termination (C).

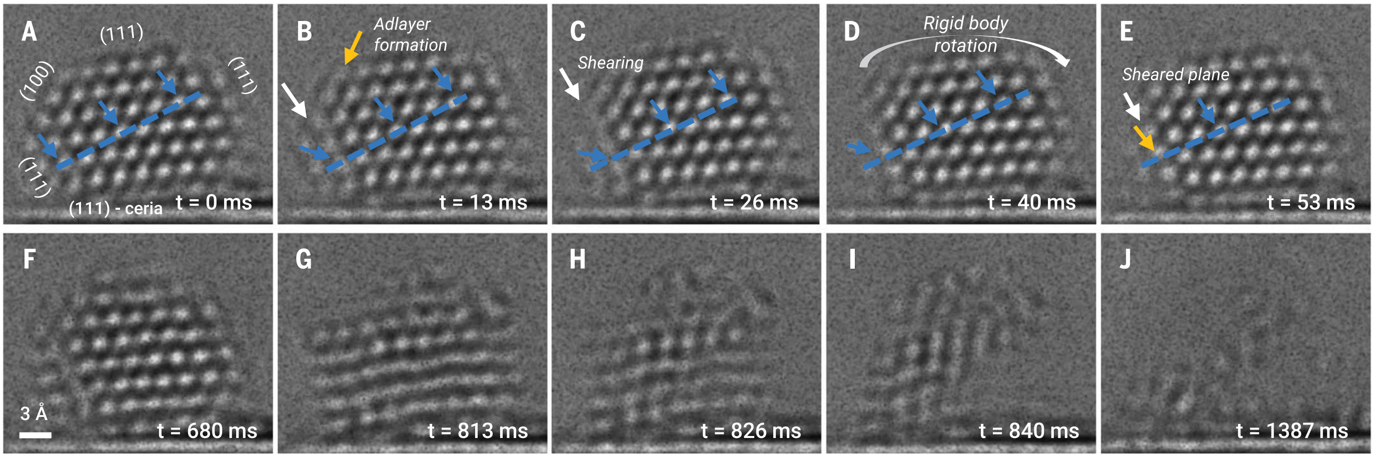

Fig. 3. Dynamics at subsurface sites and nanoparticle fluxionality. (**A** to **E**) Sequence of images of Pt nanoparticle showing the formation of a subsurface stacking fault. (A) Presheared state of the nanoparticle. Blue dotted line is perpendicular to a set of (111) planes, with the bulk showing usual ABCA stacking and blue arrows showing the location of the A layers. (B) The (111) plane (marked by white arrow) and (100) plane (marked by yellow arrow) showing streaking contrast demonstrating the onset of plane instability. (C) The (111) and (100) dynamic adlayer formation indicating that pronounced atomic motion occurred at rates beyond the frame exposure time of 13 ms. Rigid body rotation was also observed of the entire nanoparticle. (D and E) The (111) plane stabilizes in its new shifted position forming a stacking fault showing ABCB stacking (yellow arrow). The adlayers transformed back to crystallographic terminations. (**F** to **J**) Surface interface instabilities drove structural dynamics and the phase contrast images became highly fluxional. The entire particle was destabilized, which resulted in rapid changes in crystal orientation and structure.

layers. Figure 3 (and movie S5 in the supplementary materials, section 8) captures the occurrence of a crystallographic shearing event taking place on a plane just below the surface leading to the formation of a stacking fault. In this case, a (111) Pt plane slid laterally, causing the ideal face-centered cubic stacking sequence (Fig. 3A) to transform into a hexagonal close-packed surface domain (Fig. 3E and the supplementary materials, section 5). At the same time, the particle underwent a rigid body rotation of ~10° clockwise, which made the (111) Pt plane parallel to the (111) surface of the CeO_2.

The temporal evolution shows that the system passed through a transition state lasting ~13 ms (Fig. 3C), during which time the entire (111) plane showed streaked contrast characteristic of structural disorder or motion. Simultaneously, the adjacent surface layers on the left and upper left side of the particle showed adlayer contrast. This observation demonstrated that instabilities associated with surface adlayers could destabilize the crystal structure below the surface.

The adlayers renucleated into ordered crystallographic terminations as the stacking fault was created (Fig. 3, D and E) and the structure stabilized. The stabilization associated with stacking fault formation was short lived, and the particle underwent a reverse shear 600 ms later. The surface and subsurface layers then became very dynamic, which led to the entire particle becoming fluxional, manifesting as rapid changes in atomic structure, particle shape, and orientation (Fig. 3, F to J; movie S5 in the supplementary materials, section 8; and discussion in the supplementary materials, section 4). The structure present in Fig. 3J was not easy to determine. The raw data (see movie S4 raw) showed very low contrast with a sparse, rapidly changing phase contrast speckle indicative of rapid changes occurring. The denoiser picked out the stronger features of the speckle pattern, but these did not correspond to atomic columns. The particle may also have been changing more rapidly than the frame time. Each frame would then have been a superposition of images of the particle with different structures and orientations, and, for phase contrast imaging, this would wash out the contrast in the recorded frame. This entire particle fluxionality was more frequently observed in the smaller particles <1.5 nm (see movie S7 in the supplementary materials, section 8). We may hypothesize that adlayer-initiated disruptions below the surface were more likely when the surface-to-volume ratio was higher and the contact area with the oxide support was smaller, making small particles less stable.

Quantifying fluxionality

To explore this hypothesis in greater depth, we have developed an approach to quantify the order and/or disorder in images based on topological data analysis, specifically by means of summaries of persistent homology (*28*). A brief description of the approach is given in the supplementary materials, section 6. Persistent homology tracked the change in the degree of connectivity between dark (or light) pixels in a single image during intensity thresholding, and in a more ordered image, this connectivity was more persistent with thresholding. Specifically, the so-called accumulated lifetime persistent survival (ALPS) statistic acts as a measure of structural order in the image. This summary is normalized for particle size in such a way that gives a value near unity in the vacuum (corresponding to no order or contrast). An advantage of this approach is that it makes no assumptions about the form of the image (that is, the presence of atomic columns or fringes, etc.), so it can be applied to images from particles in any orientation. Applying this approach to a sequence of images from the same particle provided a quantitative measure of the order evolution with time and allowed comparison of the degrees of order between nanoparticles.

The ALPS statistic, plotted as a function of time in Fig. 4A for the particle shown in Fig. 3, had values ranging from ≥1.3, which correspond to ordered structures, to values ≤1.1, which correspond to low degrees of order. The rapid small ALPS fluctuations of ~0.1 unit were not noise but were associated with constantly changing surface structures. The plot in Fig. 4A provides a quantitative, high-level view of particle stability and explicitly shows the time that the system spends in metastable ordered states versus highly disordered states.

Particle-size effects

We applied ALPS statistics to quantitatively compare the structural dynamics in nanoparticles of different size in 23 movies (~25,000 frames) from particles in the size range 0.7

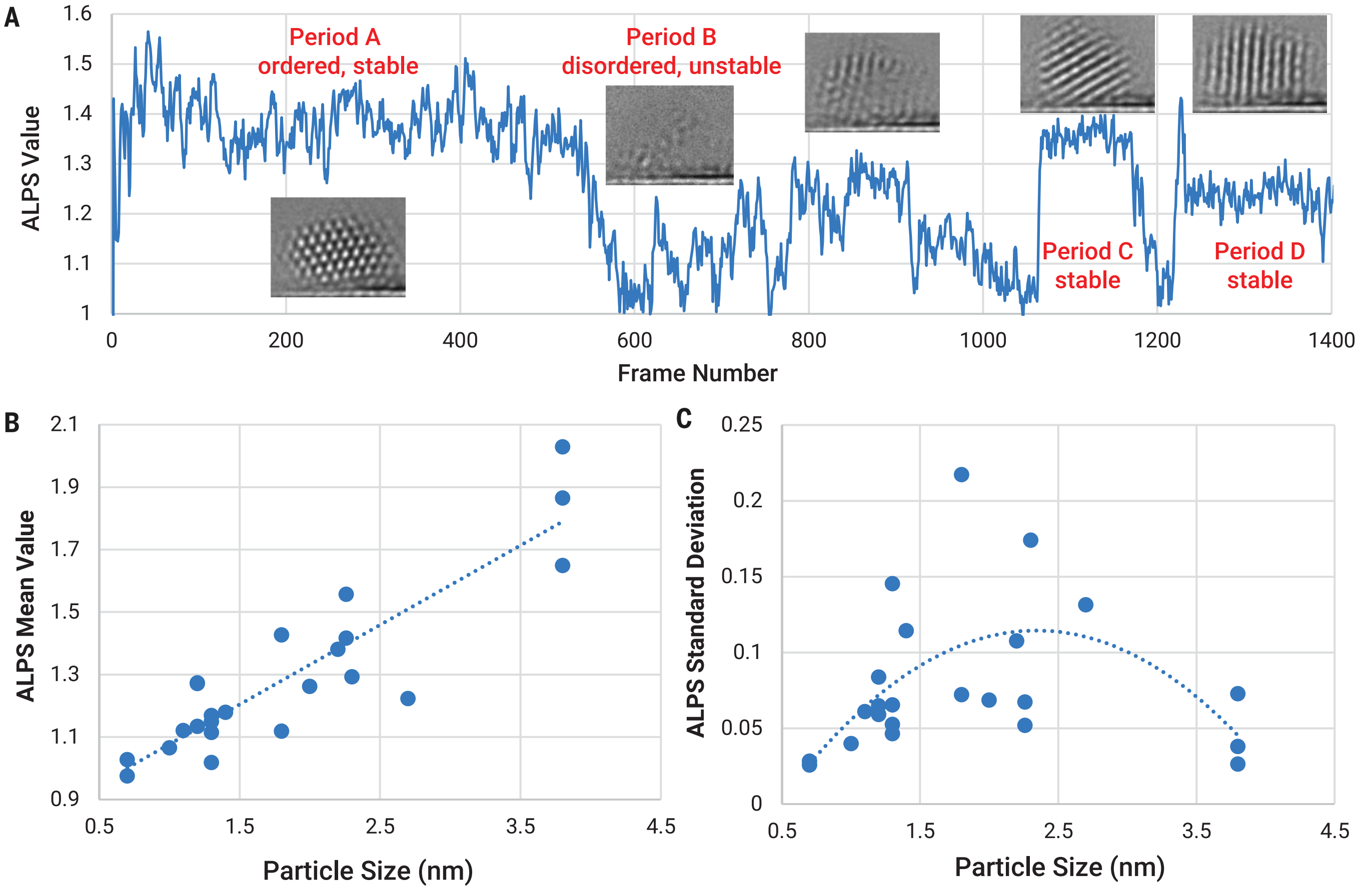

Fig. 4. Quantifying global structural dynamics in Pt nanoparticles. (**A**) The order parameter (ALPS) versus frame number (frame time = 1/75 s ~13 ms) for the same particle showing the transition from ordered to disorders configuration (inserts are typical images for each of the four stable time periods A to D). (**B** and **C**) The mean order parameter and SD as a function of particle size for different nanoparticle measured with 13-ms time resolution over periods of 8 to 15 s.

to 4 nm (for details, see the supplementary materials, section 6, and movies S6 and S7 in section 8). To simplify and facilitate the comparison between particles, the mean and standard deviation (SD) of each ALPS plot were determined and plotted as a function of particle size in Fig. 4, B and C. The mean value of the ALPS statistic showed an approximately linear dependence with particle size (and surface-to-volume ratio), quantitatively confirming the hypothesis that instability is inversely proportional to size.

The SD showed a poorly defined maximum in the size range 1.5 to 3 nm, which suggested that there were three categories of structural dynamics for the Pt particles. The first category had the largest ALPS value (>1.5) and relatively small SDs, corresponding to larger particles that remain well ordered throughout the period of observation. Although their surfaces were dynamic, their ALPS statistic was dominated by the bulk because of their small surface-to-volume ratio, and these particles remained relatively stable.

The second category had the smallest ALPS values (<1.2) and small SDs. These were particles 1.5 nm or smaller and had high degrees of disorder. Their low SDs showed that they were rarely in highly ordered states. From inspection of the denoised movies, the high degree of disorder was associated with high degrees of fluxionality. Because the particles have a high surface-to-volume ratio, fluxional surface adlayers drove fluxionality for the entire particle.

The third category showed a wide range of SDs and a wide range of ALPS values. They were predominantly intermediate-sized particles between 1.5 and 3 nm, which manifested very diverse behaviors and could either be extremely fluxional or relatively stable. The particle dynamics depended on the degree of stability of their surfaces and on the stability of the interface with the support.

The particle shown in Figs. 3 and 4 belonged to this third category and exhibited different degrees of order at different time periods. For period A in Fig. 4A, the particle shows a well-defined orientation with the support. Activation of the reverse shear (Fig. 3F) marked a period of more pronounced structural instability (period B), which manifested through large surface and interface changes.

The availability of the denoised atomic-resolution image for each ALPS point allowed the structural origin for the stability or instability transformation to be explored. For example, the degree of instability was oscillatory throughout period B, and inspection of the images shows that this was associated with a set of Pt (111) fringes (making an angle of 77° with the support) that repeatedly appeared and disappeared. The particle continuously attempted to establish a stable interfacial structure with the CeO_2 support but failed to achieve a stable configuration. The Pt particle surface was extremely fluxional throughout this process.

The particle then entered a more ordered period C, characterized by Pt (111) fringes that made an angle of ~30° with respect to the support. Another shearing operation (at frame 1141) caused the particle to enter a brief period of instability before entering period D, an ordered stable period characterized by Pt(111) fringes making and angle of ~87° with respect to the support. The transitions from metastable to unstable configurations represented a rich and complex space, but the topological analysis allowed this complexity to be quantified in time and the denoised images permitted the associated evolutionary structural pathways to be elucidated.

Discussion

Consideration of thermodynamic and kinetic factors can provide a framework from which to interpret the fluxional observations. Before exposure to CO, most of the Pt particles exhibited the thermodynamically favored Winterbottom shape consisting of (111) and (100) facets (see the supplementary materials, section 2). The structural dynamics initiated almost immediately after exposure to CO with the particles evolving away from the Winterbottom shape. The behavior was stochastic and particles in the 1.5- to 4-nm range did temporarily revisit the equilibrium shape for various periods of time. The smaller ones were too fluxional to make any strong statement about a favored shape. The disruptive and dynamic role of the chemisorbed CO on the stability of the Pt surface facets and equilibrium shape should not be underestimated. The large chemisorption energy (~1.5 eV) was associated with significant electron transfer between the metal and the molecule and disrupted the local Pt–Pt bonding, which led to enhanced Pt migration accelerating the kinetics. However, the concept of a global equilibrium shape in such an environment for small particles may be questionable. The equilibrium shape is dominated by surface energies, and the CO will cause dynamics changes in surface energies because it was diffusing on the surface and also adsorbed and desorbed with time at certain sites. For example, the local surface energy of a Pt (111) facet with 50% CO coverage will change if the coverage spontaneously changes to 40% or 60%. Consequently, the thermodynamic driving force was constantly changing on the atomic scale, and there was no well-defined Winterbottom shape.

Thermal fluctuations constantly perturbed the system, locally driving surface migration, but there was no global equilibrium shape for the system on the timescale of our observation. Any conclusion that the observed transition structures, such as stacking faults and chimney structures, are high-energy configurations may be incomplete because we are not able to directly observe the associated CO surface overlayer. The complex surface dynamics that were observed at the atomic level can be understood from a kinetic perspective by considering the Arrhenius relations governing the migration rate r ($r = A\exp(-E_a/kT)$, where k is Boltzmann's constant). Any process in or on a material with an activation energy $E_a \leq 0.7$ eV will occur many times per second at room temperature (the attempt frequency, A, can be approximated as the phonon frequency ~10^{12} Hz). Prior TEM observations of static nanoparticle surfaces at room temperature may have appeared stationary, because the image recording averaged over the atomic-level dynamics. Going to higher temporal resolution revealed that atomic-level dynamics were constantly taking place. The surface will only become truly static at absolute zero. Although the observations reported here are in CO, it seems likely that many nanoparticle surfaces may show fluxionality under a wide range of different conditions.

In conclusion, with the help of a newly developed unsupervised AI denoising algorithm and in situ electron microscopy, we made atomic-resolution observations of nanoparticle surfaces with time resolutions down to 10 ms and under a moderate electron dose. The structural dynamics of Pt nanoparticles in a CO atmosphere were observed and characterized as a function of particle size. The nanoparticle surfaces continuously transitioned between relatively stable crystallographic terminations and more active adlayers composed of rapidly diffusing Pt atoms. The atoms of the adlayer temporarily "floated" on top of the conventional crystallographic terminations and sometimes nucleated, adding a crystallographic monolayer to the surface or diffusing away. This process was continuous with the crystallographic terminations repeatedly stabilizing and destabilizing on timescales of <100 ms at room temperature. The surface structural dynamics and stress fields penetrated below the surface and led to defect formation such as stacking faults. Many of the particles, especially the smaller ones, were observed to go through extended periods of extreme structural instability. Through the application of topological data analysis, we were able to quantify and differentiate periods when the particle was in a well-ordered metastable state from the more fluxional disordered configurations. The high spatiotemporal information from the denoiser allowed the short-lived atomic-resolution elementary structural steps associated with nanoparticle transitions to be identified. The combination of AI-powered unsupervised denoising and in situ electron microscopy provides a new approach with which to investigate the field of atomic structural dynamics and stability. This will provide a new perspective for fundamental materials research by allowing functionalities to be correlated, not only to static atomic structure, but also to local structural dynamics.

REFERENCES AND NOTES

1. Y. Zhou, C. Jin, Y. Li, W. Shen, *Nano Today* **20**, 101–120 (2018).
2. D. E. Shaw *et al.*, *Science* **330**, 341–346 (2010).
3. J. L. Vincent, P. A. Crozier, *Nat. Commun.* **12**, 5789 (2021).
4. S. B. Vendelbo *et al.*, *Nat. Mater.* **13**, 884–890 (2014).
5. J. S. Kim *et al.*, *Science* **321**, 1472–1475 (2008).
6. T. LaGrange *et al.*, *Micron* **43**, 1108–1120 (2012).
7. Y. Zhang, D. J. Flannigan, *Nano Lett.* **19**, 8216–8224 (2019).
8. F. A. Cotton, *J. Organomet. Chem.* **100**, 29–41 (1975).
9. L. D. Marks, *Rep. Prog. Phys.* **57**, 603–649 (1994).
10. H.-Y. Chao *et al.*, *Chem. Rev.* **123**, 8347–8394 (2023).
11. M.-J. Xiao, H. Sun, Y. Meng, F. Zhu, *Catal. Sci. Technol.* (2024).
12. F. F. Tao, P. A. Crozier, *Chem. Rev.* **116**, 3487–3539 (2016).
13. J. R. Jinschek *et al.*, *MRS Bull.* **49**, 174–183 (2024).
14. A. Nassereddine *et al.*, *ChemCatChem* **15**, e202300434 (2023).
15. A. De Wael *et al.*, *Phys. Rev. Lett.* **124**, 106105 (2020).
16. H. Frey, A. Beck, X. Huang, J. A. van Bokhoven, M. G. Willinger, *Science* **376**, 982–987 (2022).
17. E. L. Lawrence, B. D. A. Levin, B. K. Miller, P. A. Crozier, *Microsc. Microanal.* **26**, 86–94 (2020).
18. K. Zhang, W. Zuo, Y. Chen, D. Meng, L. Zhang, *IEEE Trans. Image Process.* **26**, 3142–3155 (2017).
19. S. Mohan *et al.*, *IEEE Trans. Comput. Imaging* **8**, 585–597 (2022).
20. A. Marcos-Morales *et al.*, Evaluating unsupervised denoising requires unsupervised metrics. arXiv:2210.05553 [cs.CV] (2022).
21. M. A. van Spronsen, J. W. M. Frenken, I. M. N. Groot, *Chem. Soc. Rev.* **46**, 4347–4374 (2017).
22. A. von Oertzen, H. H. Rotermund, S. Nettesheim, *Surf. Sci.* **311**, 322–330 (1994).
23. S. R. Longwitz *et al.*, *J. Phys. Chem. B* **108**, 14497–14502 (2004).
24. D. Y. Sheth *et al.*, Unsupervised deep video denoising. arXiv:2011.15045 [eess.IV] (2020).
25. Z. R. Mansley, L. D. Marks, *J. Phys. Chem. C Nanomater. Interfaces* **124**, 28038–28043 (2020).
26. S. B. Simonsen *et al.*, *J. Am. Chem. Soc.* **132**, 7968–7975 (2010).
27. N. Panagiotides, N. I. Papanicolaou, *Int. J. Quantum Chem.* **110**, 202–209 (2010).
28. A. M. Thomas, P. A. Crozier, Y. Xu, D. S. Matteson, *Technometrics* **65**, 590–603 (2023).
29. Code for: P. A. Crozier *et al.*, Zenodo (2025); https://doi.org/10.5281/zenodo.14630448.
30. Data for: P. A. Crozier *et al.*, Zenodo (2025); https://doi.org/10.5281/zenodo.14618961.

ACKNOWLEDGMENTS

We thank ASU Research Computing and NYU HPC for providing high-performance computing resources and the electron microscopes in the Eyring Materials Center at Arizona State University. **Funding:** This work was supported by the National Science Foundation (grants OAC-1940263 and 2104105 to P.A.C. and P.H., grant CBET 1604971 to J.V., grant DMR 1840841 to M.T., grant CHE 2109202 to Y.W., grant OAC-1940097 to M.L., grant OAC-2103936 to C.F.-G., and grants OAC-1940124 and DMS-2114143 to D.S.M. and A.M.T.). **Author contributions:** P.A.C. and C.F.-G. conceived and directed the project. J.V., M.T., and P.H. acquired the TEM data. M.L., S.M., A.M.M., and S.A.K. wrote and tested the denoising codes. Y.F., M.T., and P.H. performed additional tests of the denoising codes and denoised and analyzed all the experimental data. D.S.M. and A.M.T. wrote and tested the persistent homology codes. M.T. and A.M.T. applied the persistent homology codes to the Pt nanoparticles and analyzed the results. **Competing interests:** The authors declare no competing interests. **Data and materials availability:** The denoising code (*29*) and the raw data and denoised data for Figs. 2, 3, and 4 (*30*) are available on Zenodo. All data needed to evaluate the conclusions in the this study are present in the main text or the supplementary materials.

SUPPLEMENTARY MATERIALS

science.org/doi/10.1126/science.ads2688
Materials and Methods
Figs. S1 to S7
References (*31–58*)
Movies S1 to S7

Submitted 7 August 2024; accepted 14 January 2025
10.1126/science.ads2688